AAPPS Bulletin

REVIEW ARTICLE Open Access

Strong field physics pursued with petawatt lasers

Vishwa Bandhu Pathak[1], Seong Ku Lee[1,2], Ki Hong Pae[1,2], Calin Ioan Hojbota[1], Chul Min Kim[1,2] and Chang Hee Nam[1,3*]

Abstract

Recent ultra-short high-power lasers can provide ultra-high laser intensity over 10^{22} W/cm^2. Laser fields of such extreme strengths instantaneously turn matter into plasma, which exhibits relativistic collective dynamics, thereby leading to unprecedented physical systems with potential breakthrough applications. In this article, we introduce the basic concepts and trace the progress in ultra-high intensity laser development and relativistic laser-plasma interactions, including laser-driven charged particle acceleration.

1 Introduction

"New directions in science are launched by new tools much more often than by new concepts. The effect of a concept-driven revolution is to explain old things in new ways. The effect of a tool-driven revolution is to discover new things that have to be explained," [1] said Freeman Dyson, one of the founders of quantum electrodynamics (QED) [2]. The term "tool-driven revolution" may be just the right words to describe the progress of strong field physics wherein a quantum jump in laser intensity has always led to novel physics areas.

Light intensity above 10^6 W/cm^2 became available from the very first laser invented in 1960 [3]. In the very next year, two-photon absorption [4] and second harmonic generation [5] were reported, which heralded non-linear optics. When the intensity jumped to 10^{13} W/cm^2, the resulting electric field was comparable to the atomic Coulomb field, and strongly non-linear responses of atoms began to be investigated, such as high harmonic generation and above-threshold ionization [6, 7]. A critical stage was reached when the intensity rose to 10^{18} W/cm^2. The electric field of such a high intensity light could drive electrons close to the speed of light in a fraction of an optical period. Thus, physical systems showing relativistic collectivity were realized in the labs [8, 9]. Such systems, called relativistic laser-plasmas, produce highly energetic electrons, ions, and photons. High-energy particle generation is one of the most prominent topics in strong field physics [10–14]. Currently, the record intensity values go beyond 10^{22} W/cm^2 [15–17]. At such extreme intensity, light can directly subject electrons to strong radiation reaction [18]. Furthermore, non-linear QED phenomena can occur when such an intense laser pulse collides with GeV electrons. Under such an intense field, the vacuum can behave as a dielectric, which may be probed with X-rays ([19, 20], and references therein). As the laser intensity increases further, we can expect to encounter entirely new phenomena.

In this article, we present the basic concepts and recent progress in strong field physics. First, the key technologies in ultra-intense laser development are described, and the performance of the state-of-art lasers is mentioned. Relativistic laser-plasma interactions are then explained, starting from single-electron dynamics and culminating in laser-driven charged particle acceleration, which has emerged as one of the most intensively pursued topics in this field. Finally, the main conclusions are given along with a brief mention of upcoming topics.

* Correspondence: chnam@gist.ac.kr
[1]Center for Relativistic Laser Science, Institute for Basic Science, Gwangju 61005, South Korea
[3]Department of Physics and Photon Science, Gwangju Institute of Science and Technology, Gwangju 61005, South Korea
Full list of author information is available at the end of the article

2 Ultra-high intensity lasers

An ultra-high intensity laser can serve as an excellent tool to explore novel physical phenomena. Matters exposed to extremely high intensity can exhibit exotic phenomena through laser-matter interactions. Recently, laser intensities have reached 5×10^{22} W/cm^2 [17], thanks to advanced laser technologies. In this section, the status of ultra-high intensity lasers and the key advanced technologies are presented.

Since the invention of the laser in 1960 by T. Maiman [3], new lasers with steadily increasing intensity have been built. The intensity I of the laser beam is determined by

$$I = \frac{E}{\Delta t \cdot A}, \tag{1}$$

where E is the energy, Δt the pulse duration, and A the cross-sectional area of the beam. The laser intensity can be enhanced by increasing laser energy, shortening pulse duration, or by reducing beam size. With the introduction of effective pulse shortening techniques, such as Q-switching and mode-locking, the pulse duration of a laser could be significantly shortened: a nanosecond (ns) pulse duration could be obtained by Q-switching and a picosecond (ps) or femtosecond (fs) pulse duration by mode-locking. In parallel, higher laser energy was obtained by adopting the architecture of a master oscillator combined with power amplifiers, called MOPA, where the oscillator generates a high-quality seed pulse, and power amplifiers boost the laser pulse energy. Note that amplifiers' energy scaling is limited due to non-linear effects like self-focusing induced in the medium. The refractive index of a medium exposed to a high-intensity laser pulse is given by

$$n = n_o + n_2 I, \tag{2}$$

where n_0 is the linear refractive index, n_2 the non-linear refractive index, and I the laser intensity. A high-intensity laser beam, possessing spatial intensity modulation, can split into several beamlets in a gain medium due to n_2 which generate hot spots due to self-focusing, leading to damage of laser media and optical components. Such damages during amplification can be avoided by increasing the size of the laser beam in successive amplifier stages, but the beam expansion is limited by the size of the available large amplifier medium and other optical components. Figure 1 shows the chronological increase in laser intensity. After the introduction of the mode-locking technique, no significant breakthrough was achieved in enhancing the laser intensity until 1985. Till then, the only method to increase the laser intensity gradually was to increase the size of laser amplifier media.

In 1985, D. Strickland and G. Mourou, Nobel laureates in physics (2018) [21], demonstrated an innovative amplification technique called Chirped-Pulse Amplification (CPA) [22]. Figure 2 shows the concept of CPA. In the CPA technique, an ultra-short seed pulse is stretched to a duration in the range of picosecond or even ns by a pulse stretcher in order to avoid non-linear effects by maintaining the laser intensity below a critical level, called damage threshold, during amplification. The stretched seed pulse is then amplified from ~nJ to ~J or

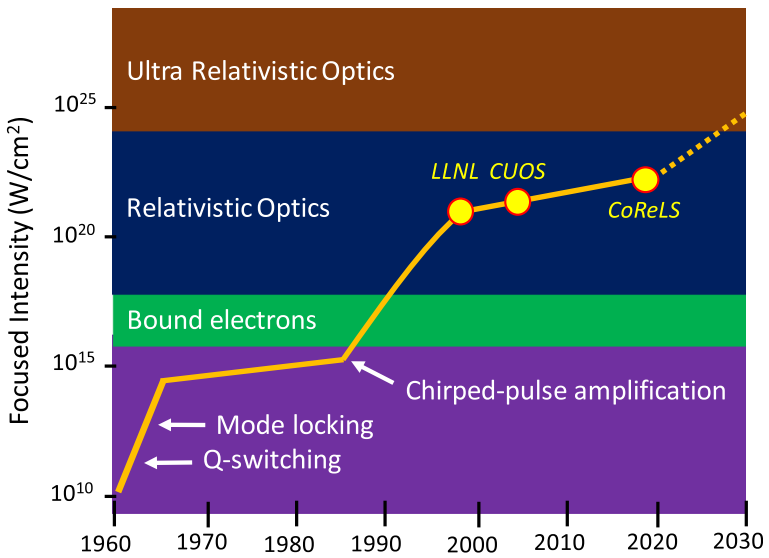

Fig. 1 Chronological increase in laser intensity

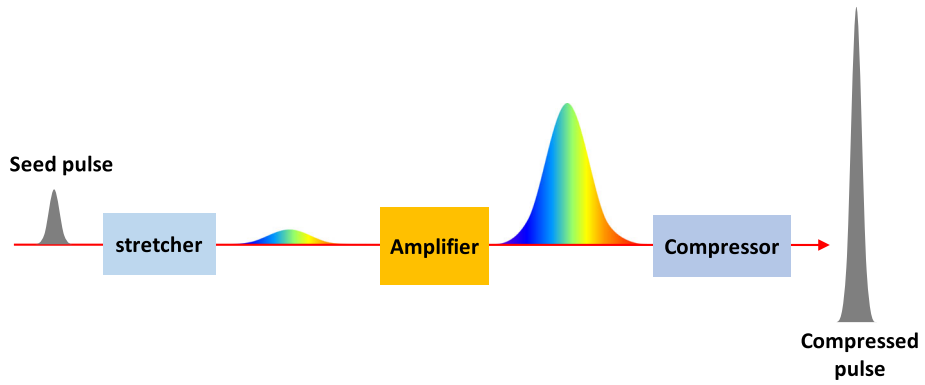

Fig. 2 Concept of chirped pulse amplification (CPA)

higher energy, and the amplified pulse is compressed to the initial pulse duration by a pulse compressor. The CPA technique has opened a new era of ultra-high intensity lasers by overcoming the damage issues due to non-linear effects.

2.1 Chirped pulse amplification (CPA) laser

An ultra-high intensity laser using the CPA technique is generally composed of a femtosecond oscillator, a pulse stretcher, amplifiers, and a pulse compressor, as shown in Fig. 3. In a Ti:Sapphire CPA laser, a femtosecond oscillator generates an ultra-short seed pulse with a pulse duration of 5–20 fs through Kerr-lens mode-locking, in which mode-locking occurs due to the Kerr effect. The laser pulse is then stretched to several picoseconds or nanoseconds by a grating pulse stretcher to extract high energy from amplifiers without optical damage. The first CPA laser employed a long fiber to stretch a seed pulse [22], and the stretched pulse was compressed by two parallel gratings (Treacy type) [23]. Although the pulse compression was successfully implemented in the first CPA laser, high-order spectral chirps could not be appropriately eliminated because the dispersion of the fiber stretcher and that of the grating compressor did not match well. A new type of pulse stretcher based on gratings (Martinez type) was then utilized to match the dispersion of the Treacy-type compressor [24]. Nowadays, an Öffner type stretcher has been adopted in most of the ultra-high intensity lasers, in which only reflective optics are used in order to avoid the chromatic aberration, as shown in Fig. 3 [25].

With technological advances, TW and PW CPA lasers have been developed around the world. For an ultra-high power CPA laser, the gain medium of amplifiers with a broadband gain and a high energy storage is desired to produce ultra-short high energy pulses. Among the gain

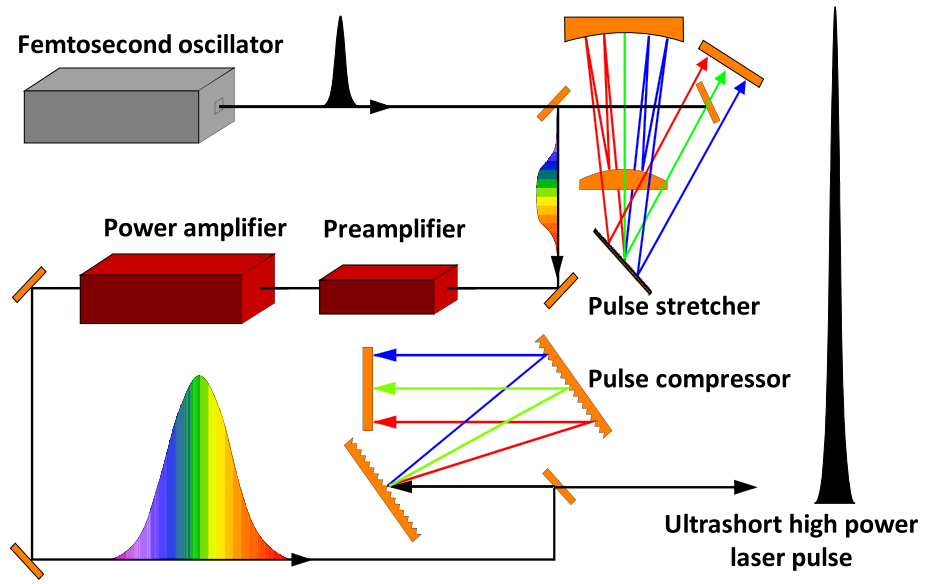

Fig. 3 High power femtosecond CPA laser

media, Nd:glass and Ti:sapphire have been mainly employed for ultra-high intensity lasers. Nd:glass has a moderate bandwidth and a large saturation fluence of 4 J/cm^2. For high energy output in ultra-high intensity lasers, the amplifier chain consists of several amplifiers such as preamplifiers and power amplifiers, as shown in Fig. 3. In 1994, an ultra-short multi-TW Ti:sapphire laser with a pulse duration of 30 fs was reported [26]. The first PW CPA laser was demonstrated with a hybrid Ti:sapphire-Nd:glass laser by M. Perry et al., generating an output power of 1.5 PW with an energy per pulse of 660 J and a pulse duration of 440 fs [27]. Currently, a 10-PW Nd:glass CPA laser is being constructed at ELI-beamlines [28]. Ti:sapphire has a very large bandwidth and a moderate saturation fluence of 0.9 J/cm^2. A Ti:sapphire CPA laser can generate ultra-short high power pulses in a table-top system. Besides, the thermal conductivity of Ti:sapphire is so good that Ti:sapphire CPA lasers can be operated at a high repetition rate. Since the reporting of a 30-fs, 4-TW Ti:sapphire laser at 10 Hz in 1994 [26], the output power of Ti:sapphire lasers has increased rapidly. A 0.84-PW Ti:sapphire laser was developed at Kansai Photon Science Institute (KPSI) in 2003 [29], and a 1.0-PW Ti:Sapphire laser was first demonstrated at Advanced Photonics Research Institute (APRI) in 2010 [30]. Recently, multi-PW Ti:sapphire lasers have been or are being constructed at several institutes: 4.2 PW at the Center for Relativistic Laser Science (CoReLS) (Fig. 4) [31], 10 PW at Shanghai Institute of Optics and Fine Mechanics (SIOM) [32], and 10 PW at Extreme Light Infrastructure-Nuclear Physics (ELI-NP) [33].

In addition to the CPA technique, a stretched pulse can be amplified by using three-wave mixing, called Optical Parametric Chirped Pulse Amplification (OPCPA), proposed and demonstrated by Dubietis et al. [34]. Figure 5 shows the conceptual diagram of an OPCPA laser, where a non-linear crystal is used as an amplification medium instead of a gain medium like Ti:Sapphire or Nd:glass. A PW-class OPCPA laser with an output power of 0.2 PW was first developed at the Institute of Applied Physics (IAP) in 2006 [35], and a 4.9-PW OPCPA laser was established at the China Academy of Engineering Physics (CAEP) in 2017 [36]. The OPCPA has many advantages compared to the conventional CPA due to the parametric process. The OPCPA can generate a broadband spectrum to accommodate few-cycle pulses in non-collinear geometry, while, in CPA lasers, the gain bandwidth is limited due to the effects of gain narrowing and gain depletion. Large non-linear crystals are available, and transverse amplified stimulated emission does not occur in the OPCPA process. Besides, a high-energy (kJ) Nd:glass laser, developed for laser fusion, can be used as a pump source. These advantages enable the construction of lasers with ultra-high power output exceeding 10 PW [37].

On the downside, the OPCPA has the disadvantage of low efficiency. The OPCPA is a parametric process and,

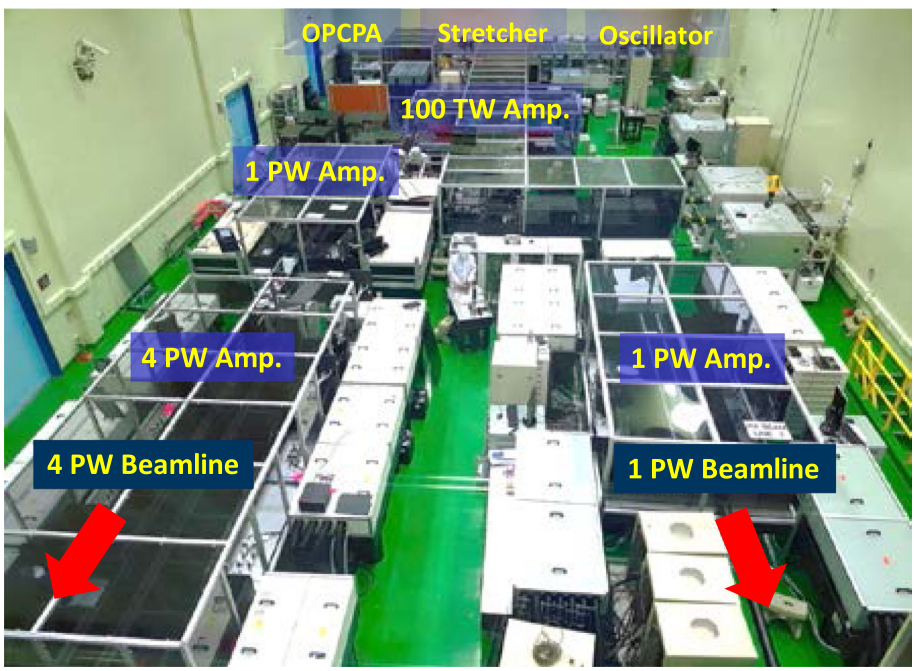

Fig. 4 Multi-petawatt Ti:sapphire laser facility at CoReLS. The 1-PW beamline was constructed in 2010, and the 4-PW beamline in 2017

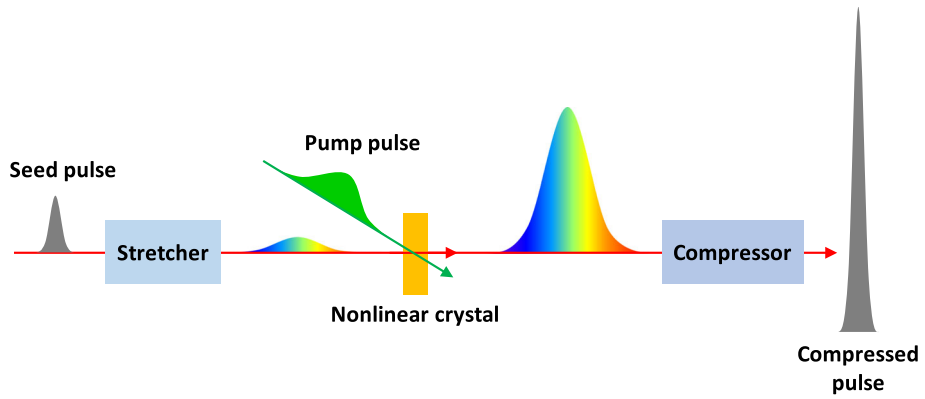

Fig. 5 Concept of optical parametric chirped pulse amplification (OPCPA)

hence, the efficiency of signal generation is reduced by the back-conversion process, i.e., the sum-frequency generation between signal and idler. In addition, the gain depends considerably on pump intensity and, hence, the output beam quality of the OPCPA laser is seriously affected by the pump beam profile. Consequently, the pump laser beam needs to be properly prepared to obtain ultra-high intensity at the focus.

2.2 Focused laser intensity

Focused laser intensity is one of the critical factors affecting physical processes in laser-matter interactions. Focused laser intensity can be maximized if the focused beam size is minimized for given laser energy and pulse duration. A laser beam usually contains wavefront aberrations acquired during the propagation from an oscillator to a target, which deteriorates the focal spot image. Such aberrations are induced by several sources. Firstly, optics such as mirrors, windows, waveplates, and even gain media are not perfect, and they distort the wavefront. In particular, large-aperture optics, such as large size mirrors and gratings, can induce large aberrations. Secondly, the thermal effect in amplifiers can also induce aberrations in the wavefront of the laser beam. Finally, beam pointing and air turbulence need to be taken into account. The induced wavefront aberrations can lead to larger focal spot, and, hence, to lower focused intensity. For correcting the wavefront and achieving high focused intensity, the wavefront should be flat, which can be realized by using an adaptive mirror system, which compensates for the wavefront aberrations by using a deformable mirror. In 2004, laser intensity of 0.7×10^{22} W/cm^2 was achieved by focusing a 45-TW laser with an F/0.6 off-axis paraboloid mirror after correcting the wavefront [38]. Recently, laser intensity of 1.1×10^{22} W/cm^2 was reported at ultra-high intensity laser facilities: J-Karen-P laser at QST [15] and SULF laser at SIOM [16]. In 2019, CoReLS produced a record laser intensity of 5.5×10^{22} W/cm^2 by employing two deformable mirrors located before and after a compressor [17]. The first deformable mirror, installed before the compressor, flattened the phase to prevent the spatiotemporal coupling effect in pulse compression. The second deformable mirror, placed after the compressor, corrected the wavefront error due to the large aperture optics used in the beam transportation and the tight focusing after the compressor. Figure 6 shows the phase map of the ultra-intense laser beam at a target chamber before and after the correction by the adaptive mirror system. As shown in Fig. 6b, the adaptive mirror system successfully corrected the wavefront to yield a nearly diffraction-limited focal spot.

2.3 Temporal contrast

In the investigation of laser-matter interactions, the temporal contrast is critical, especially for solid targets. Nowadays, the focused laser intensity at targets can be higher than 10^{22} W/cm^2. The temporal contrast of a laser, defined as the intensity ratio between the main pulse and pre- and post-pulses, should be taken into account because laser pulses with an intensity exceeding 10^{10} W/cm^2 can induce damage on thin solid targets. The typical temporal profiles of ultra-intense laser pulses are shown in Fig. 7. The pre- and post-pulse components of an ultra-intense laser pulse are composed of three parts: femtosecond pre- and post-pulses, pre- and post-pedestal with a duration of several tens of picoseconds and amplified spontaneous emission (ASE) of a nanosecond duration. In general, the post-pulses of femtosecond duration are produced by surface reflections in transmission optics such as waveplates and windows. Pre-pulses can be induced by post-pulses during amplification and pulse compression due to the phase modulation induced by the non-linear refractive index given by Eq. (2) [39]. The pedestals are generated due to several causes: spectrum clipping, spectral phase distortion in a

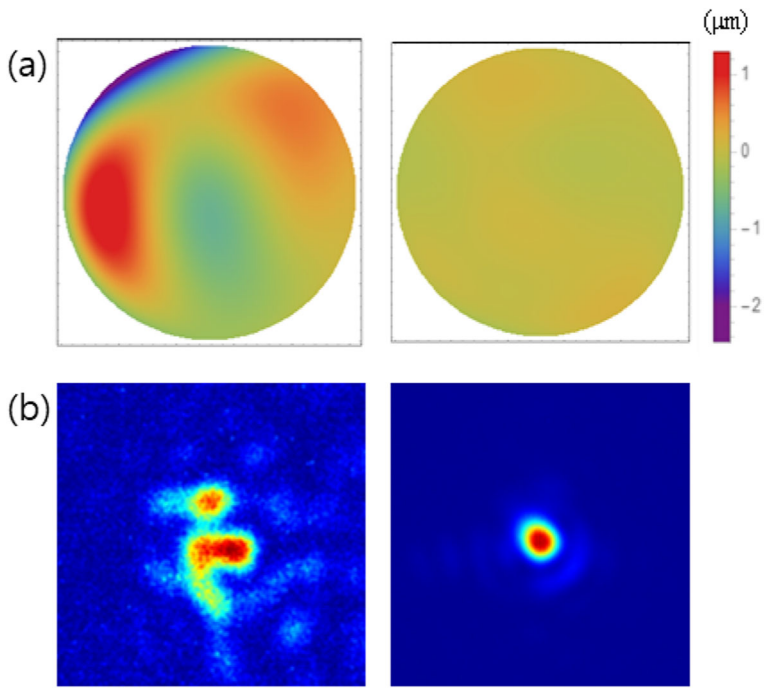

Fig. 6 **a** Wavefront maps before (left) and after (right) wavefront correction. **b** Focal spot images before (left) and after (right) wavefront correction

stretcher [40], scattering from gratings in the stretcher and compressor [41], etc. Finally, the ASE mainly originates from the oscillator background and the incomplete Pockels cell switching.

For cleaning the pre-pulse components of a laser pulse, special techniques are employed, such as saturable absorption [42], cross-polarization wave generation (XPW) [43], OPCPA, and plasma mirrors [44]. In particular, the XPW has been widely employed in the

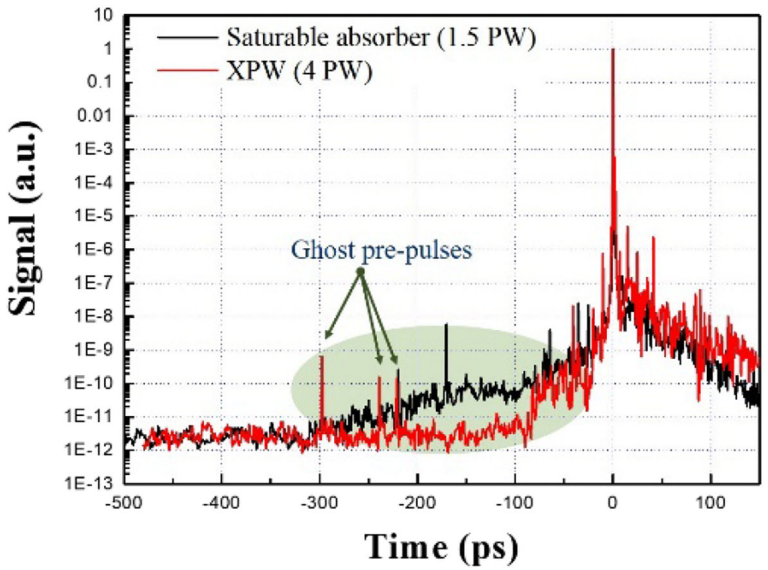

Fig. 7 Temporal contrasts of the ultra-high intensity lasers at CoReLS. The 30 fs, 1.5 PW laser employed saturable absorbers in the frontend, while the 20-fs 4-PW laser adopted an XPW stage

frontend of ultra-high intensity lasers, because it can improve the contrast ratio and also broaden the spectral width [31]. A plasma mirror is utilized to enhance the contrast ratio after pulse compression, where weak prepulses pass through an anti-reflection window glass, while the main femtosecond pulse is reflected by the plasma generated by the leading edge of the main pulse. Choi et al. reported that the contrast ratio of a multi-PW laser reached 10^{-17} up to 160 ps and 10^{-12} up to 2 ps before the main pulse by using a double plasma mirror system, which enabled irradiation of tens-of-nanometers-thick polymer targets at an intensity of about 10^{22} W/cm^2 [45].

We have reviewed the configuration and characteristics of ultra-high intensity lasers based on the CPA technique. The output power of such lasers has reached 10 PW, and even higher power lasers are being constructed and planned. The laser intensity also increased rapidly, and it exceeded 10^{22} W/cm^2 due to the development of ultra-high power lasers and related laser technologies. Ultra-high intensity lasers are paving the way for the exploration of novel physics such as strong-field QED through laser-matter interactions in the unprecedented intensity regime.

3 Relativistic laser-plasma interactions

An intense laser pulse, propagating through a plasma, undergoes an evolution of its field structure in time and space. Understanding the laser dynamics in plasmas has been an active area of research for more than half a century [46–50] due to its relevance to laser-driven fusion [51], laser wakefield acceleration [32, 35–37], ion acceleration [52, 53], radiation generation [54], and parametric instabilities [50, 55]. Here, we focus mainly on electron and ion acceleration in high-intensity laser-produced plasmas.

3.1 Electron acceleration

Plasma-based accelerators, first proposed by Tajima and Dawson [56], have been intensively investigated and shown to deliver multi-GeV [57, 58] electrons in a distance which is orders of magnitude shorter than that in conventional accelerators. Recent particle-in-cell (PIC) simulations in a Lorentz-boosted frame [59] predicted electron bunch energy over 10 GeV in a meter-scale plasma using next-generation 10 PW lasers. Accelerating wakefields of nearly 50 GeV/m have been observed experimentally in plasmas [60], which is almost 1000 times higher than the fields employed in conventional accelerators. Recently, by modifying the spectral properties of PW laser pulse, Kim et al. [58] have obtained 2-GeV electron beams in a 1-cm plasma, indicating even higher, up to 200 GeV/m, accelerating gradients. In laser or plasma wakefield acceleration (LWFA/PWFA), a short laser pulse or ultra-relativistic electron beam propagates through an underdense plasma and excites plasma waves [49, 56] that can trap and accelerate electrons to ultra-relativistic energy. Here, we focus only on laser-driven wakefield acceleration of electrons. To understand the process, we begin by analyzing the single particle motion in non-relativistic and relativistic electromagnetic fields.

3.2 Single particle motion in an electromagnetic field

Before discussing the highly non-linear and complicated collective dynamics of relativistic laser plasma interactions, we introduce a simple and basic concept of the single particle motion in a laser electromagnetic field. Under the action of a plane electromagnetic wave having an electric field $\vec{E} = E_0 \exp[-i(\omega_0 t - k_0 z)]\hat{x}$, an electron oscillates with velocity $\vec{v}$ of amplitude $v = eE_0/(m_e\omega_0)$, where e and m_e are the electron charge and mass, and E_0, ω_0, and k_0 are the laser field amplitude, laser angular frequency and wavenumber, respectively.

We shall define the normalized vector potential, a dimensionless parameter, as the ratio of the maximum electron velocity exerted by the laser-field in a single laser cycle to the speed of light in vacuum (c): $a_0 = eE_0/m_e\omega_0 c = eA_0/m_e c^2$, where A_0 is the corresponding vector potential amplitude of the laser. This dimensionless parameter can also be seen as the ratio of the electron kinetic energy gained in a single cycle of the field to the rest mass energy of the electron. The normalized vector potential determines whether the motion is relativistic or not: for $a_0 > 1$, the electron dynamics becomes relativistic. By solving the full set of the Lorentz equation with a plane electromagnetic field, we find that the electron trajectories are described by $x = (a_0 c/\omega_0)\cos(\omega_0 t - k_0 z)$ and $z = (a_0^2/4)[ct - (c/2\omega_0)\sin(2\omega_0 t - 2k_0 z)]$. Seen in the frame of reference moving with the velocity $c \cdot a_0^2/(a_0^2 + 4)$, an electron exhibits the well-known figure-of-8 motion in the $x - z$ plane (Fig. 8c): $x^2(1 - x^2\omega_0^2/c^2) = 16z^2$ [61]. The transverse (longitudinal) component of the trajectory is proportional to a_0 (a_0^2). As a consequence, the longitudinal motion, which is negligible in the non-relativistic cases ($a_0 \ll 1$), becomes relevant as a_0 increases, as shown in Fig. 8d.

3.3 Ponderomotive force and relativistic pulse propagation

In experimental conditions, due to the finite size of a laser pulse, plane-wave solutions are not sufficient to fully understand the dynamics. In the non-relativistic case with an infinite plane wave, no space-charge is formed due to electron drift since an electron undergoes a simple harmonic motion around its initial position, regardless of its position. However, this is not true for a

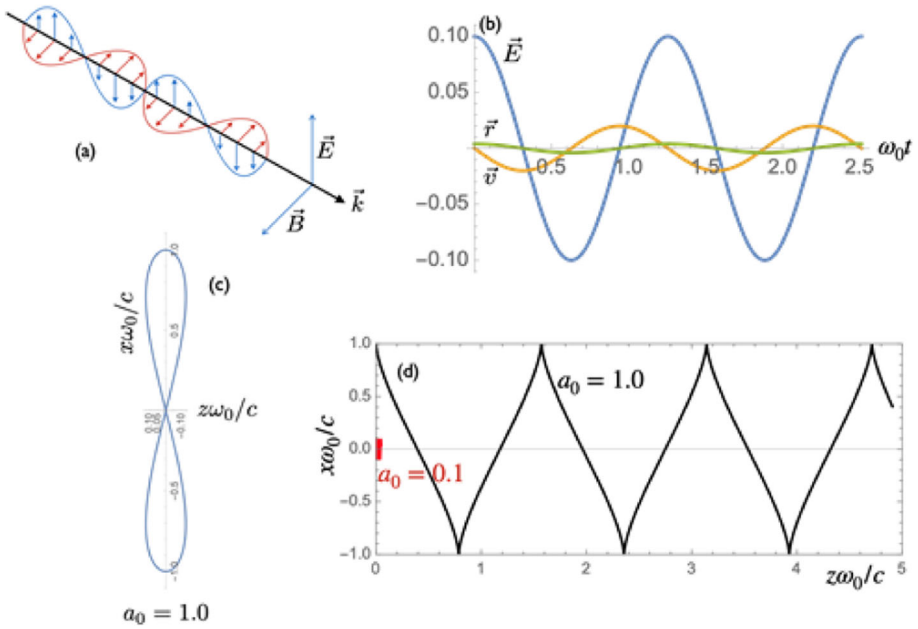

Fig. 8 Single particle motion in a plane electromagnetic wave: ***a*** electromagnetic field of a laser and ***b*** profiles of the electric field (blue), electron velocity (yellow), and electron transverse position (green) with respect to $\omega_0 t$, ***c*** electron trajectory in the frame of reference moving with the electron longitudinal drift, and ***d*** electron motion in space for non-relativistic ($a_0 = 0.1$) and relativistic ($a_0 = 1.0$) cases

finite laser beam, where, due to the finite transverse size of the beam, a non-linear force, called ponderomotive force, acts on an electron along the direction of decreasing laser intensity. For a linearly polarized laser, the ponderomotive force acting on an electron can be written as $\overrightarrow{F}_p = -(m_e c^2/4)\nabla a_0^2$. Thus, for a laser beam with a spot size W_0 and envelope profile $a^2 \sim \exp(-x^2/W_0^2)$, the laser pulse, propagating through a plasma, pushes electrons away from the axis of the laser beam (the orange line in Fig. 9a), creating a space charge in the background of nearly stationary ions (Fig. 9b). If the laser pulse is sufficiently long, a stationary state is reached wherein the Coulomb force due to the charge separation balances the ponderomotive force on electrons, and a plasma channel is formed, as shown in Fig. 9c.

When the relativistic regime is reached, due to the relativistic mass effect, $m_{\text{eff}} = m_e\gamma = m_e\sqrt{1 + a^2/2}$, the ponderomotive force is modified to $\overrightarrow{F}_p = -m_e c^2 \nabla\gamma$ [49, 61]. The refractive index of the plasma is also modified to $\eta = \sqrt{1 - \omega_p^2/\omega_0^2\gamma}$, where $\omega_p = \sqrt{4\pi n_e e^2/m_e}$ is the plasma frequency. The dominant contributions to the plasma refractive index, relevant to the propagation

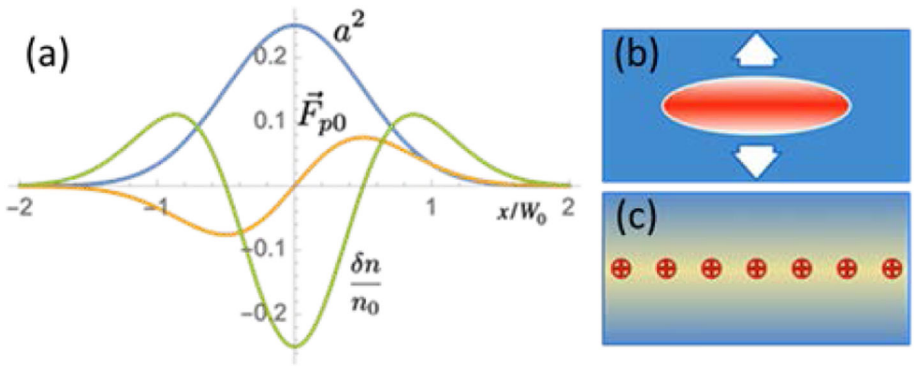

Fig. 9 Plasma channel formation due to the ponderomotive force of a laser pulse. **a** The transverse laser profile (square of the normalized vector potential, blue), the corresponding ponderomotive force (orange), and the electron density (green) as a function of x/W_0. **b** A cartoon of the laser pulse with the direction of the ponderomotive force marked by arrows. **c** The resulting channel formed due to immobile ions

of short laser pulses, come from the ponderomotive force and effective mass non-linearities. The non-linear coupling between the laser pulse and the plasma dynamics can lead to several processes, such as laser self-steepening [62], self-compression [63], self-focusing [64], and self-modulation ([49, 64] and references therein). For a Gaussian laser pulse, due to the relativistic effects, the refractive index decreases as we go away from the laser axis. This causes the laser beam to focus, and the process is known as relativistic self-focusing (Fig. 10a). Similarly, due to the electron density modification by the ponderomotive force, the refractive index is lower away from the laser axis than the on-axis refractive index, which also leads to ponderomotive self-focusing (Fig. 10b). The consequence of self-focusing is that the laser pulse can propagate as a parallel beam over a distance far greater than the Rayleigh length, overcoming the restriction imposed by diffraction due to the finite beam size of the laser pulse. This phenomenon of relativistic self-guiding requires a laser with power more than the critical power given by $P_{\mathrm{cr}} = 17(\omega_0^2/\omega_p^2)$ GW [49, 50, 64]. For a laser pulse with power less than the critical power for self-focusing, an external guiding structure, such as a parabolic plasma channel, is needed to guide the laser to a longer distance [49, 57].

3.4 Wakefield excitation

Here, we begin with the basic understanding of wakefield excitation by a laser pulse. As the laser pulse propagates through a plasma and pushes electrons away from the axis by the ponderomotive force, a space charge is created due to stationary ions. If the laser pulse is short enough, the ions do not move, and the electrons are pulled back towards the axis due to the Coulomb force after the laser pulse has moved out of the region. This process triggers an electron density modulation just behind the laser, called laser wakefield. One-dimensional equations governing the density modulation (δn) of electrons, and the corresponding electrostatic potential (ϕ), due to a non-relativistic ($a_0 \ll 1$) linearly polarized laser pulse, can be written as [49]

$$\left(\frac{\partial^2}{\partial t^2} + \omega_p^2\right)\frac{\delta n}{n_0} = c^2\nabla^2\frac{a^2}{2}, \tag{3}$$

and

$$\left(\frac{\partial^2}{\partial t^2} + \omega_p^2\right)\phi = \frac{\omega_p^2 a^2}{2}. \tag{4}$$

The solutions for the density modulation and the corresponding electric field are obtained as

$$\frac{\delta n}{n_0} = \frac{c^2}{\omega_p}\int_0^t dt' \sin\left[\omega_p(t-t')\nabla^2\frac{a^2(\vec{r},t')}{2}\right], \tag{5}$$

and

$$\frac{\vec{E}}{E_0} = -c\int_0^t dt' \sin\left[\omega_p\left(t-t'\right)\nabla\frac{a^2(\vec{r},t')}{2}\right]. \tag{6}$$

The plasma wave is generated with a modulation frequency ω_p, and $E_0 = m_e c\omega_p/e = 96\sqrt{n_0[\mathrm{cm}^{-3}]}$ [V/m] is the cold non-relativistic wave breaking field, which suggests that within the plasma longitudinal accelerating fields can get generated which are around three orders of magnitude higher than that in conventional RF accelerators. Tajima and Dawson proposed to utilize such strong fields excited by a short pulse laser to accelerate electrons.

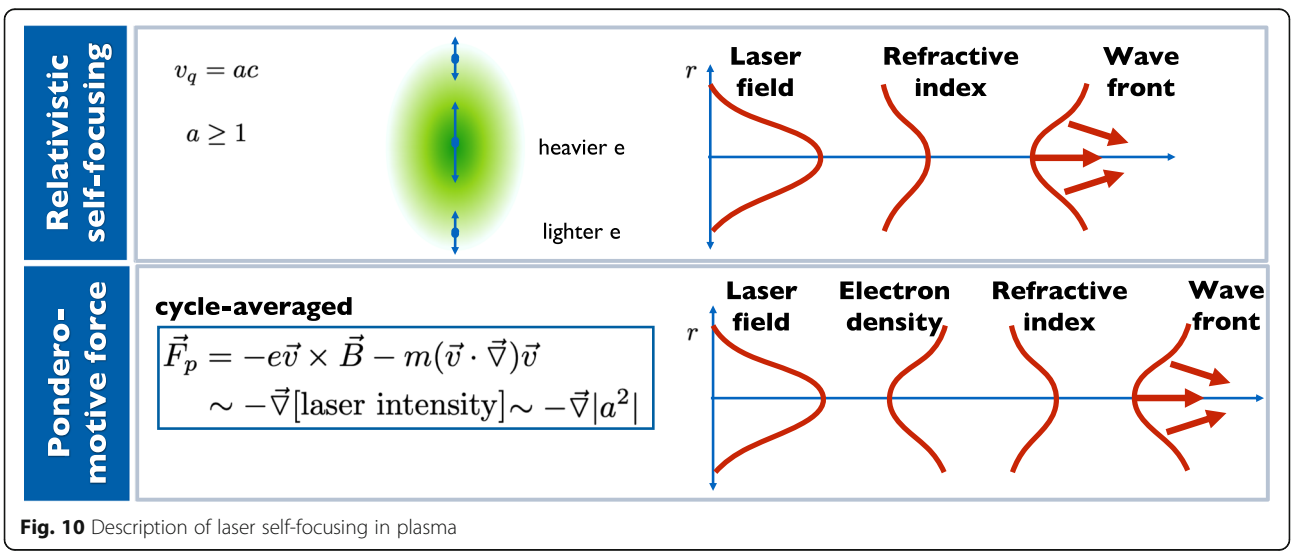

Fig. 10 Description of laser self-focusing in plasma

Density modulations excited by a short laser pulse, $a = a_0 \cos(\omega_0 t) \sin(\pi t/\tau_L)$, for $0 < t < \tau_L$, is plotted in Fig. 11 for various laser pulse lengths showing that maximum wakefield can be generated when the gradient scale length of laser intensity ($\sim a^2$) matches the plasma wavelength $\lambda_p = 2\pi c/\omega_p$

For the relativistic case, i.e., $a > 1$, the linear theory of wakefield excitation breaks down because waves become highly non-linear. In the non-linear regime, the equation for the wakefield potential can be written as [49]

$$k_p^{-2} \frac{\partial^2 \phi}{\partial \xi^2} = \gamma_p^2 \left[\beta_p \left\{ 1 - \frac{\gamma_\perp^2}{\gamma_p^2 (1+\phi)^2} \right\}^{-1/2} - 1 \right], \quad (7)$$

where $k_p = \omega_p/c$, $\xi = z - u_p t$, $\gamma_\perp^2 = 1 + a^2$, $\gamma_p^2 = (1-\beta_p^2)^{-1/2}$, and $\beta_p = u_p/c$. $u_p \approx c$ is the phase velocity of the plasma wave. The corresponding density profile and electron beam Lorentz factor γ can be written as [49]

$$\frac{n}{n_0} = \gamma_p^2 \beta_p \left[\left\{ 1 - \frac{\gamma_\perp^2}{\gamma_p^2 (1+\phi)^2} \right\}^{-1/2} - \beta_p \right], \quad (8)$$

and

$$\gamma = \gamma_p^2 (1+\phi) \left[1 - \beta_p \left\{ 1 - \frac{\gamma_\perp^2}{\gamma_p^2 (1+\phi)^2} \right\}^{\frac{1}{2}} \right]. \quad (9)$$

Figure 12 shows the plot of the non-linear response of a plasma to a laser pulse with $a_0 = 1.5$, having a Gaussian temporal profile, a pulse length equal to half the plasma wavelength, and $\omega_0/\omega_p = 10$. Such an intense pulse excites a non-linear wakefield with sharp density spikes (green line in Fig. 12) and a sawtooth-shaped longitudinal electric field ($E_z = -E_0 \partial\phi/\partial\xi$) (yellow line in Fig. 12). In such a regime, the wavelength as well as the electric field in the wakefield can significantly increase beyond the limitations of the linear regime.

3.5 Blowout regime of laser wakefield acceleration

In the case of even higher laser intensities ($a_0 > 3$), a laser pulse can push all the electrons from its vicinity, which creates a bubble-shaped structure entirely devoid of electrons just behind the laser. It was first shown in PIC simulation by Pukhov et al. [65]. This regime is also known as the blowout regime of laser wakefield acceleration [66, 67]. Experimentally, this is the regime suitable for particle acceleration. The maximum acceleration field that can be achieved in the blowout regime varies as $E_z^{max} \approx E_0 \sqrt{a_0}$. The large accelerating field associated with the blowout, shown in Fig. 13, can trap and accelerate plasma electrons (self-injection), leading to the generation of quasi-monoenergetic multi-GeV electrons. In addition, the linear transverse focusing force associated with the bubble is ideal for the generation of X-ray radiation, as the accelerated electron beam executes betatron oscillations in the ion channel [54, 68, 69].

In Fig. 14, we show three-dimensional particle-in-cell simulation results with OSIRIS [70] to describe the laser wakefield acceleration (LWFA). For the simulation, we consider the propagation of a Gaussian-shaped laser pulse, with $a_0 = 6$, laser spot size $W_0 = 30$ μm, and pulse length $\tau_L = 20$ fs, through a homogeneous plasma with $n_0 = 3 \times 10^{18}$ cm^{-3}. As the laser pulse propagates in the plasma and excites a non-linear wakefield structure (Fig. 14a), electrons are accelerated by the wakefield, and they co-propagate with the laser pulse with a phase velocity nearly equal to the group velocity of the laser front $v_g \approx c(1 - 3\omega_p^2/2\omega_0^2)$ [67], due to the localized etching of the pulse around its rising edge [71]. In this case, we observe instantaneous self-injection (Fig. 14b) due to the

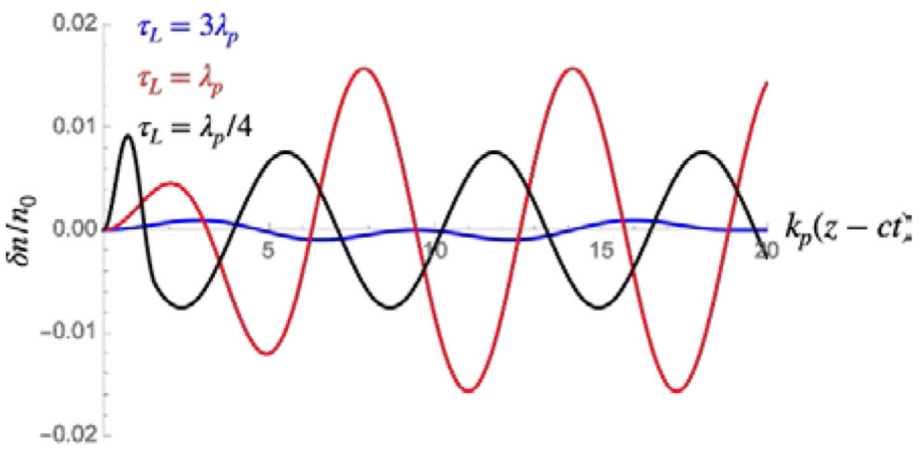

Fig. 11 Density modulation excited after the laser pulse for three values of pulse length, $c\tau_L = \lambda_p/4$ (black), λ_p (red), and $3\lambda_p$ (blue). $k_p = \omega_p/c$

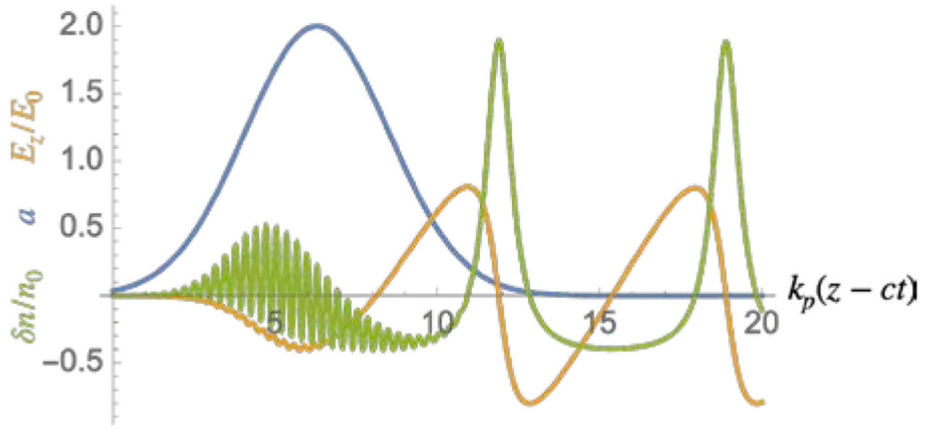

Fig. 12 Wakefield excitation in the non-linear regime. Laser pulse profile in blue, electron density modulation in green, and corresponding longitudinal field is shown in yellow

strong wakefield [66, 67, 72]. As the laser pulse gets self-focused (Fig. 14f), its intensity increases, and further electron injection occurs due to the fast expansion of the bubble (Fig. 14c) [73]. The corresponding longitudinal field evolution is plotted in Fig. 14g–i, and electron longitudinal phase-space is plotted in Fig. 14j–l, highlighting the early stage of self-injection and acceleration. The fast expansion leads to higher charge but poor beam quality in terms of energy spread and energy tail (Fig. 14o).

In LWFA, acceleration length is one of the important parameters determining the final electron energy. For a self-guided laser pulse, the effective acceleration length is limited either by the laser etching (depletion) length $L_{\text{etch}} = (\omega_0^2/\omega_p^2)c\tau_L$ or by the dephasing length $L_d = (4/3)(\omega_0^2/\omega_p^2)a_0 c/\omega_p$ [67]. As is clear from the expressions, the acceleration length, and hence the energy gain, is higher at lower plasma density because the ratio ω_0/ω_p is larger. In contrast, particle trapping is better at higher plasma density because the required longitudinal electron momentum for self-injection also scales with ω_0/ω_p [67]. Therefore, the electron injection and the acceleration length are the competing factors in the optimization of plasma density for LWFA in a single-stage process.

In order to overcome the problem of uncontrolled self-injection, various methods to induce electron injection into the bubble by external means have been

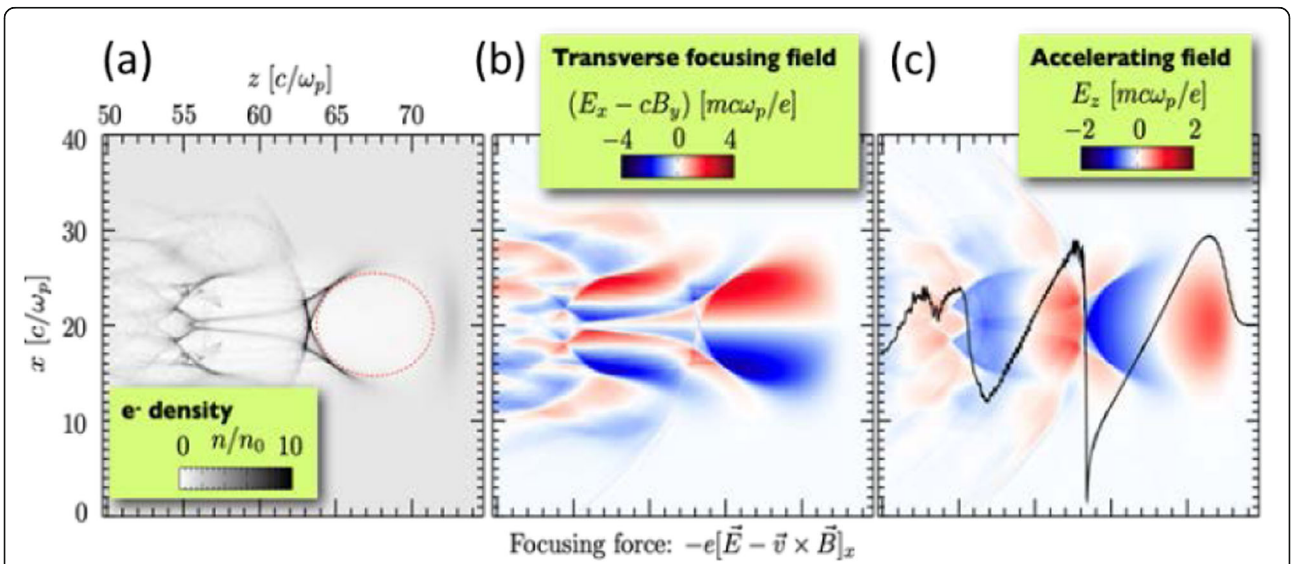

Fig. 13 Blowout regime of laser wakefield acceleration. Electron density profile in **a** shows the bubble structure, **b** shows the transverse focusing field for the electrons, and **c** shows the longitudinal electric field distribution

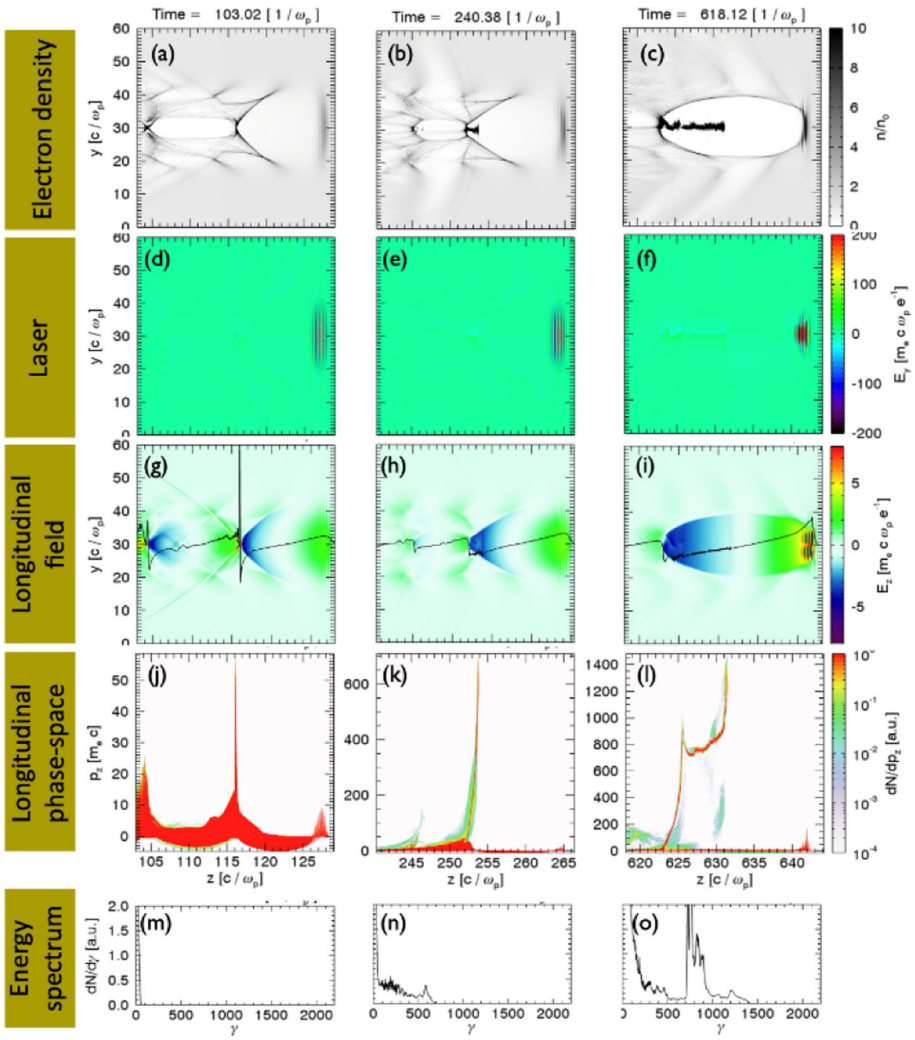

Fig. 14 Description of laser wakefield acceleration showing the evolution of wakefield excited by the laser and corresponding electron energy with $c/\omega_p = 3$ μm ($1/\omega_p = 10$ fs). Electron density is plotted in **a**, **b**, **c**; laser electric field in **d**, **e**, **f**; longitudinal electric field (and on-axis lineout) in **g**, **h**, **i**; longitudinal phase-space (z, p_z) in **j**, **k**, **l**; and electron energy spectrum is plotted in **m**, **n**, and **o**

developed. Some of these methods are short density down-ramp, ionization injection, nano-particle assisted electron injection, transverse magnetic field assisted injection, and through the beating structures associated with counter- or cross-propagating lasers.

The energy gain in LWFA for a single stage is given by [67]

$$E_n[\mathrm{GeV}] = 1.7 \left(\frac{P[\mathrm{TW}]}{100}\right)^{\frac{1}{3}} \left(\frac{10^{18}}{n_0[\mathrm{cm}^{-3}]}\right)^{\frac{2}{3}} \left(\frac{0.8}{\lambda_0[\mu\mathrm{m}]}\right)^{\frac{4}{3}}, \tag{10}$$

where P is laser power, n_0 is plasma density, and λ_0 is laser wavelength. According to the energy scaling, derived for the condition where dephasing and depletion lengths are matched, and the laser spot size (W_0) equals $2\sqrt{a_0}c/\omega_p$ [67], the electron energy is seen to depend strongly on the plasma density. However, as mentioned earlier, as the plasma density is reduced while keeping the laser power fixed, the electron energy should increase, but the increase in the cut-off momentum for self-injection as well as the lack of self-guiding places a limit on the electron energy. In such cases, using a capillary plasma medium, which provides a parabolic plasma channel for external guiding, the laser guiding length (equivalently the acceleration length) can be enhanced significantly, thus increasing the electron energy to the current record of 7.8 GeV [57].

It has been observed theoretically [74] as well as proved experimentally [58] that, by fine-tuning the spectral profile of a laser pulse for given laser and plasma parameters, the electron energy and charge can be significantly improved. Specifically, a positively chirped laser pulse can excite a stronger wakefield,

and in experiments such a laser pulse was observed to provide very stable electron beam having 2 GeV energy [58].

3.6 All-optical dual-stage laser wakefield acceleration

To enhance the energy gain in LWFA, dual-stage LWFA [75, 76] has been proposed with a short, high-density plasma in the first stage (injector stage) and a long, low-density plasma in the second stage (accelerator stage). The dual-staged LWFA can be achieved either by a single laser pulse propagating through two plasma media [53, 77] or by two independent laser pulses focused separately on two plasma media [78–80]. All these methods for dual-staged LWFA require two separate plasma media. Manipulating the laser frequency to realize a multi-stage LWFA is considerably more challenging. There are growing interests in all-optical control of LWFA, by manipulating optical properties of the driving laser pulse [58, 74] or by composing multiple laser pulses [81–83]. Pathak et al. [84] have explored an innovative solution to this limitation by proposing to use a two-color laser pulse to create the injector and accelerator stage in a single homogeneous plasma column. In this model, the leading pulse, at the fundamental frequency, acts as an injector, and the trailing laser pulse, at the second harmonic, works as an accelerator or booster. The analytical expression for the energy scaling of all-optical dual stage LWFA is derived in the matched regime. PIC simulations with OSIRIS [70] demonstrated that quasi-mono-energetic multi-GeV electron bunch can be obtained with three times higher gain as compare to single stage LWFA. It was also shown that a 10-GeV electron beam can be achieved by two-color laser pulses with the input laser power of 0.6 PW.

The energy scaling for all-optical dual-stage laser wakefield acceleration can be written as [84]

$$E_d[\mathrm{GeV}] = G_d E_n = 1.7 G_d \left(\frac{P[\mathrm{TW}]}{100}\right)^{\frac{1}{3}} \left(\frac{10^{18}}{n_0[\mathrm{cm}^{-3}]}\right)^{\frac{2}{3}} \left(\frac{0.8}{\lambda_0[\mu\mathrm{m}]}\right)^{\frac{4}{3}} \quad (11)$$

where $G_d = (1-\alpha)^{1/3} + 2^{4/3}\,\alpha^{1/3}$ is the extra gain provided by the dual stage acceleration. $\alpha = P_{2\omega_0}/P$ is ratio of the second harmonic power ($P_{2\omega_0}$) to the total laser power (P). For $\alpha = 0.05$ to 0.9, G_d varies slowly from 2.0 to 3.0, providing a stable gain factor. For $\alpha = 0$ and $G_d = 1$, the energy scales the same as shown by Lu et al. [66]. However, for the same total laser input power, the dual stage scheme can significantly enhance the acceleration gain by a factor between 2 and 3. As a result, the two-color laser pulses with $P_{\mathrm{in}} = 1$ PW, now available from PW laser facilities, can produce 10-GeV electron bunches for $\alpha = 0.3$.

3.7 Experimental investigation of laser wakefield acceleration

The results obtained in the initial LWFA experiments, proving the generation of quasi-mono-energetic electrons in the bubble regime, prompted the development of numerous laser-driven acceleration schemes and configurations. Due to reliance on high laser power to achieve multi-GeV electron energy, the highest electron energies have been produced so far using PW-class lasers [85].

The work on multi-GeV schemes is of interest both from an accelerator perspective as well as for potential studies on laser-driven radiation sources and fundamental strong field physics. The availability of high intensity laser pulses ($I > 10^{18}$ W/cm^2) coupled to existing GeV electron beams will enable studies on laser-electron collisions. From these studies, one will be able to carry out in-depth investigations on non-linear inverse Compton scattering and radiation-reaction effects, and other strong field quantum electrodynamics phenomena. Such collisions can produce 10 s and 100 s of megaelectron volt gamma photons, which in turn will stimulate research on nuclear photonics and various detection systems.

A robust scheme for controlling the properties of multi-GeV electron beams is based on the adjustment of the spectral phase of the laser pulse. Such results were investigated experimentally [58, 86], and the works showed that energy, charge, and stability of the electron beams can be improved by adjusting the group delay dispersion (GDD) and third-order dispersion (TOD) of the spectral phase.

At CoReLS, we performed experiments on multi-GeV electron acceleration, producing energies above 3 GeV. In order to enhance the beam quality, we performed in-depth studies of the effects of GDD and TOD on electron acceleration. We used a PW beamline (800 nm) with a pulse duration of 22 fs, a pulse energy of 29 J on target inside the Airy disk. The PW beam was focused to a beam waist of 50 μm using a spherical mirror with focal length $f = 12$ m (F/40) and generated an intensity of $I = 4 \times 10^{19}$ W/cm^2 ($a_0 = 4$). The laser beam was focused into an adjustable gas cell of 50–100 mm length developed in-house [87]. For acceleration, the medium was composed of 99% helium and 1% neon, to facilitate electron self-injection.

An overview of the target chamber and experimental area for LWFA studies is presented in Fig. 15. The PW beam was focused, through a holed mirror shown in Fig. 15a, onto the gas cell. After the acceleration, the electron beam profile was imaged on a scintillating (Lanex1) screen, and then the beam was spectrally dispersed by an electron spectrometer with a 30-cm magnet (B = 1.33 T). After exiting the magnet, the dispersed

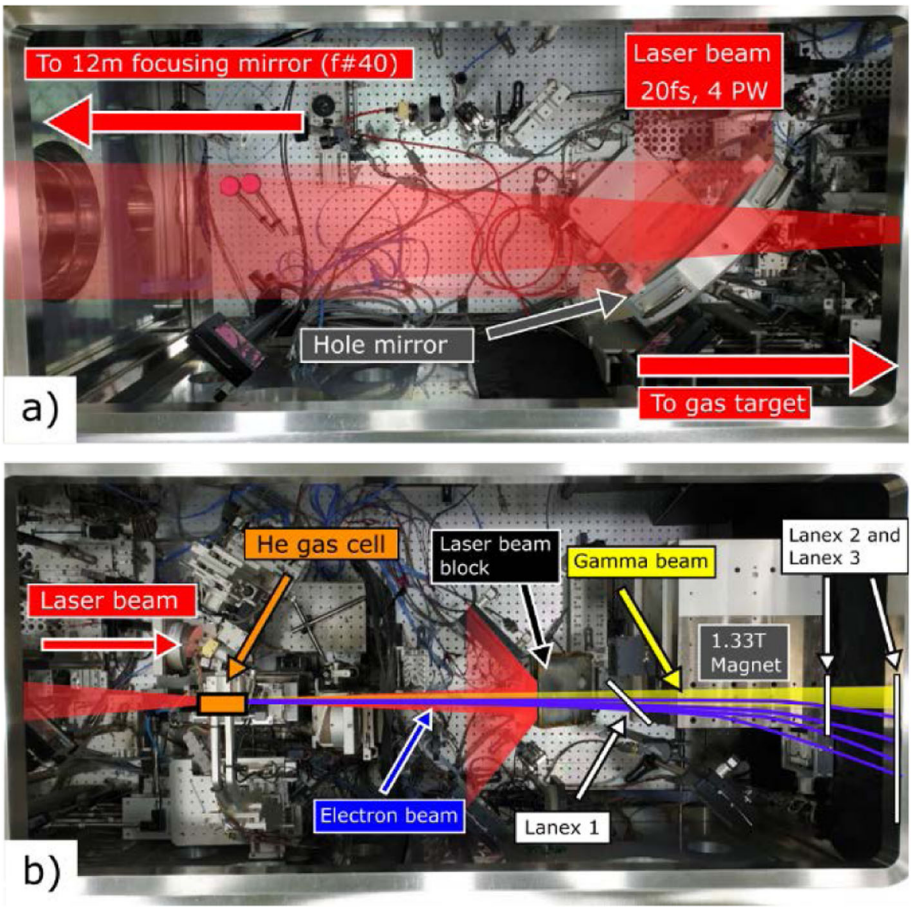

Fig. 15 Top view of the experimental chamber for LWFA at CoReLS. **a** Overview of laser beam transport and focusing to the target. **b** Setup of the target area and diagnostic of electrons after acceleration

electron beam propagated through two other scintillating screens (Lanex2 and Lanex3) for energy measurement. This three-screen setup allowed a correct spectral calibration of electron beam energy [88]. Other diagnostics for plasma (imaging, shadowgraphy, and optical emission spectra) and laser beam profile monitoring were installed outside the vacuum chamber. Secondary gamma-rays produced during LWFA experiments, such as bremsstrahlung, betatron radiation, and inverse Compton scattering radiation, were also measured outside the vacuum chamber.

Two acousto-optic dispersive filter systems (Dazzler, Fastlite) and a self-referencing spectral interferometer for phase measurement (Wizzler, Fastlite) were used for the spectral phase control. The results of the electron beam optimization in Fig. 16 clearly show the effects of GDD. For GDD < 0 (− 300 fs^2/− 400 fs^2), the electron beam energy is about 0.9 GeV, while tuning the GDD to positive values of around + 500 fs^2 allows the energy to be increased up to 1.5 GeV. The charge also got increased, and the stability of beam generation improved significantly. In this way, we were able to produce beams with low divergence (< 2 mrad), pointing fluctuations below 5 mrad, and energies above 2 GeV.

Future development of electron beam stabilization and optimization techniques will seek to increase the electron beam energy above 5 GeV using tailored density profiles and novel injection and acceleration schemes [89]. We will thus be able to employ high-quality and high-energy beams for further applications in laser-electron collisions and studies on fundamental physical processes.

3.8 Ion acceleration

Energetic ion beams have drawn great attention due to the wide range of applications, including hadron cancer therapy, electromagnetic field diagnostics in plasma, and the production of warm dense matter through isochoric heating [13]. Laser plasma accelerators of ions are among several efforts to develop a compact inexpensive high energy ion beam source. As more powerful lasers

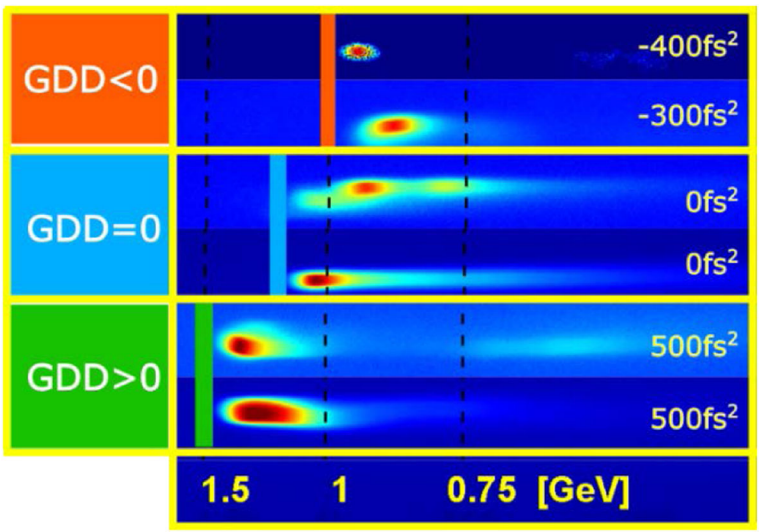

Fig. 16 Effects of group-delay dispersion on the energy of electron beams in experiment. Spectra of electron beams are shown for GDD < 0 (– 400 fs^2, – 300 fs^2), GDD = 0 (0 fs^2, 0 fs^2) and for GDD > 0 (500 fs^2, 500 fs^2)

have been developed, research is being conducted to accelerate an ion beam by irradiating solid targets with a high-intensity laser of short pulse duration [52, 90, 91].

3.9 Target normal sheath acceleration

The target-normal sheath acceleration (TNSA) mechanism of laser-driven high-energy ion generation has been widely investigated. The TNSA mechanism is illustrated schematically in Fig. 17. In this mechanism, a linearly polarized laser pulse illuminates a solid density target of a few micron thickness. When a hot plasma is generated from the front surface of a thin solid target by focusing on it an ultra-high intensity laser pulse, energetic electrons are pushed into the target. When these electrons move out of the rear surface of the target, a strong electrostatic field is formed between the target and the energetic electron cloud, called sheath field. This strong electrostatic field ionizes and accelerates protons and ions at the rear surface, resulting in energetic proton and ion beams. In TNSA of protons, the protons usually originate from water molecules due to surface contamination.

The hot electrons heated by an intense laser play a key role in accelerating ions. There are several heating mechanisms producing energetic electron streams passing through the target. Basically, electrons oscillate

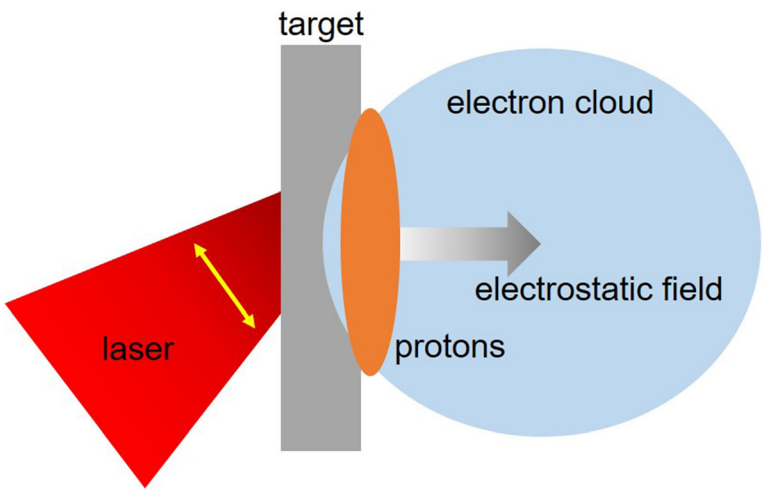

Fig. 17 Schematic illustration of the target normal sheath acceleration mechanism. A solid density target with a thickness of a few microns is irradiated with a P-polarized laser pulse

under the influence of the laser electric field at angular frequency ω of the laser. Since the electron density of the solid target is highly overdense, the laser pulse gets reflected from a thin layer at the target front surface, called as skin depth, and cannot propagate deep into the target. When a P-polarized laser pulse interacts with the target, an electron is pulled out of the target surface into the vacuum during the first half cycle of the oscillating electric field and, in the next half cycle, the electron is pushed back into the target. Following the re-entry into the target, the electron is no longer influenced by the laser field, and it delivers its energy to the target. If this electron has enough energy to pass through the target, then it escapes out of the target from its rear surface as a free particle. For an S-polarized laser beam or for the case of normal incidence, electrons oscillate parallel to the target surface. This oscillation gives rise to an oscillating electric current and, in turn, a $\mathbf{j} \times \mathbf{B}$ force, which oscillates at 2ω in the lowest order. The $\mathbf{j} \times \mathbf{B}$ force generates hot electron bunches every half cycle and drives them into the target.

The ion beams accelerated by TNSA shows characteristic features. We assume a Boltzmann distribution for the generated hot electrons,

$$n_e = n_{e0} \exp(e\Phi/k_B T_e), \tag{12}$$

where n_{e0} is the initial electron density of the target, Φ is the electrostatic potential, and T_e is the electron temperature. The maximum energy of the accelerated ions can then be written as [92],

$$E_{\max} = 2T_e \left[\ln\left(\tau + \left(\tau^2 + 1\right)^{1/2}\right)\right]^2, \tag{13}$$

where $\tau = \omega_{pi} t_1/(2e)^{1/2}$ is the normalized acceleration time, ω_{pi} is the ion plasma frequency, and t_1 is the effective acceleration time. The energy spectrum of the ions accelerated by the TNSA mechanism shows a thermal distribution with a sharp cut-off at the maximum energy. Experiments and numerical simulations reveal that the maximum energy scales as $E_{\max} \propto I^{1/2}$.

The TNSA mechanism has been studied in detail through experiments, numerical simulations as well as theory [13]. At the Advanced Photonics Research Institute, Gwangju Institute of Science and Technology, a series of experiments were performed to generate high energy protons and test the energy scaling of the protons with respect to the laser and target parameters [53]. In this campaign, protons with a maximum energy of 45 MeV were obtained by focusing a laser beam of intensity 3.3×10^{20}W/cm^2 on 10-nm-thick polymer targets. A clear understanding of the dynamics in this case was obtained by three-dimensional particle-in-cell simulations. From these experiments, a transition in the scaling of the maximum proton energy from $E_{\max} \propto I^{1/2}$ to $E_{\max} \propto I$ was observed at around $I = 2.0 \times 10^{20}$W/cm^2 when the intensity of linearly polarized laser pulses was varied from 5.0×10^{19}W/cm^2 to 3.3×10^{20}W/cm^2.

The TNSA mechanism is robust against changing laser and target conditions because it does not require a finely specified experimental setup. The weak point of this mechanism is the scalability with the laser intensity as mentioned before. It is not adequate for ion generation with energy > 100 MeV/u. The thermal distribution of the energy spectrum is, however, suitable for applications such as time-resolved proton radiography.

3.10 Radiation pressure acceleration

The light sail radiation pressure acceleration (LS RPA) mechanism of ions was proposed as a promising candidate to generate high-quality ion beams by using ultra-intense laser pulses [93, 94]. In this mechanism, the momentum of a driving laser is directly transferred to a target resulting in an efficient energy conversion. In 1D approximation, the RPA is explained by a perfect mirror model. As shown in Fig. 18, the radiation pressure due to an intense laser pulse pushes all the electrons in the target to form a compressed thin layer of electrons, resulting in a strong electrostatic field between the electron layer and the ions, which then pulls the ions. In this model, the acceleration is stable when the radiation pressure (P_{rad}) is equal to the electrostatic pressure (P_{es}) created by the thin layer of electrons [95],

$$P_{\mathrm{rad}} = 2RI/\mathrm{c} \approx P_{\mathrm{es}} = 2\pi(en_0 l)^2, \tag{14}$$

where R is the reflectivity of the laser pulse in the rest frame of the target, I is the intensity, c is the speed of light, n_0 is the electron density, and l is the target thickness. For a laser pulse with a normalized vector potential a_0, this "optimal condition" is given by

$$a_0 = \pi \frac{n_0 l}{n_c \lambda}, \tag{15}$$

where n_c is the critical plasma density and λ is the laser wavelength. From (15), it is seen that, for a laser with an intensity of 10^{21}W/cm^2, the optimal target thickness is tens of nanometers with an electron density of a few hundred times the critical density. Under this condition, the ion acceleration is stable, and a quasi-monochromatic energy spectrum is expected.

The use of a circularly polarized (CP) laser pulse can mitigate the stringent experimental requirements in RPA. When a CP laser is incident normally on a target, there is no oscillatory $\mathbf{j} \times \mathbf{B}$ force, but a steady radiation pressure exists, reducing the generation of hot electrons. In addition, for practical applications of RPA, the

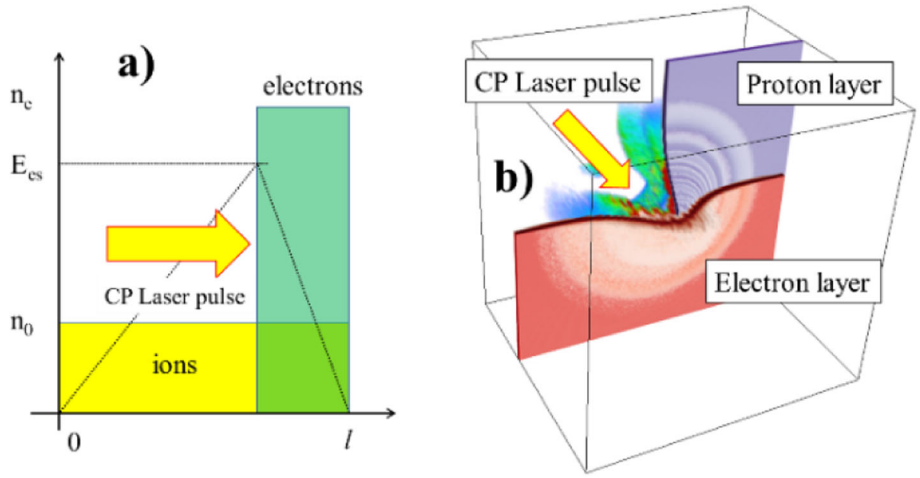

Fig. 18 a Schematic illustration of the radiation pressure acceleration mechanism. A circularly polarized laser pulse pushes electrons in a plasma with thickness *l* and initial density n_0 as a whole, compressing them to a thin layer with density n_e, and then the electrostatic field between electrons and ions pulls the remaining ions. **b** Density distributions of electrons and protons from a three-dimensional particle-in-cell simulation for the radiation pressure acceleration

thickness of a target should be very small. Since such a target can be easily destroyed by a prepulse arriving before the main ultra-high intensity pulse, the contrast ratio between a prepulse and the main pulse must be extremely high. A plasma mirror has been shown to enhance the contrast ratio by attenuating prepulses and amplified spontaneous emission existing with a main ultra-high intensity laser pulse; the double plasma mirror system developed at CoReLS has been shown to produce a contrast ratio of the laser pulse as low as 10^{-17} up to 160 ps and 10^{-12} up to 2 ps before the main pulse [45], which has enabled the use of polymer targets as thin as 5 nm.

At the CoReLS, IBS, the RPA was clearly demonstrated by using its PW laser [96]. In the proton acceleration experiment, the scaling of maximum proton energy with laser intensity and polarization at an intensity range of 10^{20}W/cm^2 was investigated by applying short, intense high-contrast laser pulses on thin F8BT polymer targets [97]. The resulting spectra for protons and ions are shown in Fig. 19. We successfully generated proton beams with the maximum energy of 93 MeV by applying 30 fs CP laser pulses with an intensity of 6.1×10^{20}W/cm^2 to 15-nm-thick polymer targets. Even though the proton spectra are broad and modulated, the optimal condition agreed well with the RPA theory. The maximum proton energy from a 20-nm target irradiated with a linearly polarized laser pulse of an intensity 7.0×10^{20}W/cm^2 was 67 MeV, which is considerably lower than that obtained using the CP laser. The RPA mechanism was confirmed by the quadratic scaling of maximum proton energy with laser intensity, optimal thickness condition, the polarization dependence of proton energy scaling, and finally the 3D particle-in-cell simulations for the experimental condition.

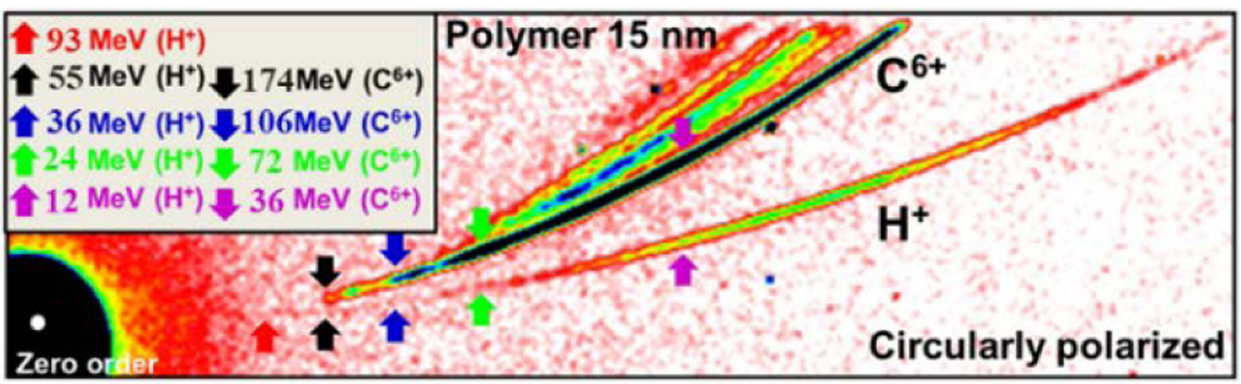

Fig. 19 Thomson parabola image from the RPA experiments at CoReLS. The spectral image of proton and carbon ions was obtained from a 15-nm-thick F8BT target irradiated with a circularly polarized laser pulse of an intensity of 6.1×10^{20} W/cm^2

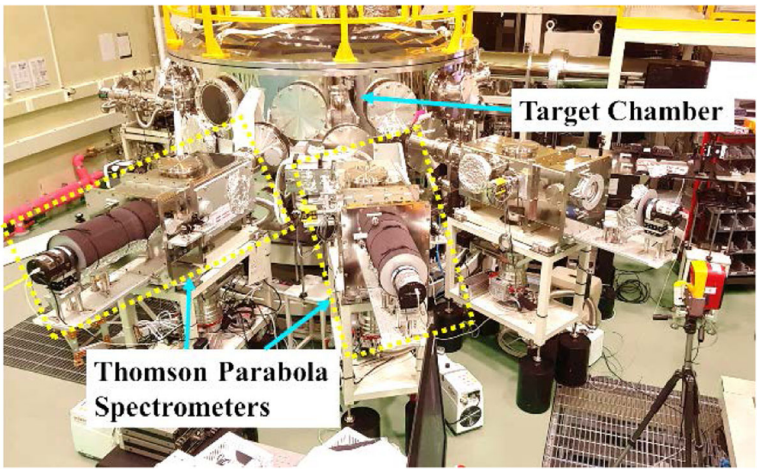

Fig. 20 Target chamber for ion acceleration experiments at the CoReLS. The Thomson parabola spectrometers used for the detection of proton spectra are marked

The PW target chamber for ion acceleration at CoReLS is shown in Fig. 20. In the target chamber, thin proton-rich solid targets were driven by femtosecond, PW laser pulses to generate high energy protons and ions. Thomson parabola spectrometers (TPS) were installed to measure proton and ion spectra with charge-to-mass resolution. A microchannel plate with a phosphor screen, imaged to a 16-bit charge-coupled device camera, was used to record ion traces.

In the multi-dimensional scenario, the RPA mechanism is known to be vulnerable to the Rayleigh-Taylor instability [98]. Due to the spatial laser intensity profile, a portion of the thin target, of the size of the pulse spot, is pushed forward, resulting in a cocoon-shaped structure. The front surface of the target is no longer normal to the laser electromagnetic field. In this oblique irradiation geometry, the incident and reflected electromagnetic fields overlap and get modulated. The modulation of the pulse results in target breaking, and then the RPA does not work anymore. The Rayleigh-Taylor instability grows further and kills the acceleration completely. The use of multi-species target was proposed to overcome the instability [99, 100]. In the proposed schemes, the layer of heavier ion species is retarded, thus preventing the instability from acting on the relatively lighter ions in the front layer of the target which gets accelerated by the RPA.

With the development of ultra-high power lasers in several institutes around the world, the laser-plasma-based ion accelerator has emerged a promising candidate for a compact inexpensive equipment to produce high quality ion beams.

4 Conclusion

This article has reviewed the basic concepts and recent progress in ultra-high intensity laser development and relativistic laser-plasma interactions. Clearly, CPA and OPCPA techniques are seen to be essential for building ultra-intense lasers. For achieving maximum intensities, the wavefront is corrected using adaptive mirrors and low-F/# focusing mirrors. Moreover, an ultra-high temporal contrast, achieved using plasma mirrors, is crucial to prevent damaging the ultra-thin targets before the arrival of the main pulse. The current state-of-art lasers have achieved intensities over 10^{22} W/cm^2 and contrasts better than 10^{-12}.

In relativistic laser-plasma interactions, strong nonlinearity shows up even in the single-electron dynamics, in contrast to the non-relativistic case. When a relativistically strong laser pulse propagates through an underdense plasma, it experiences self-focusing and excites a wakefield. The wakefield tightly follows the driving laser pulse and can act as a moving accelerator for electrons. In the laser wakefield acceleration scheme, electrons can be accelerated to energies above a GeV in a few centimeters. When a relativistically strong laser pulse is reflected by an overdense plasma, it transfers its energy and momentum to the plasma. At low intensities, the transferred energy is mostly in the form of electron thermal motion, and the resulting sheath field can be used to accelerate protons to tens of megaelectron volt. However, at optimally high intensities, the transferred energy can be mostly in the form of electronic collective motion. The resulting charge separation can accelerate protons more efficiently to hundreds of megaelectron volt. The acceleration of particles in relativistic laser-plasmas is a prominent outcome of relativistic collective dynamics, and it also has the potential to be a breakthrough particle acceleration technology. Recently, the laser electron acceleration was used to investigate strong-field QED [18–20, 101–103] and generate electron-positron plasmas [104], which are exciting upcoming topics in

strong field physics. With ultra-intense lasers, we can now explore many new areas of physics.

Acknowledgements
This work was supported by IBS (Institute for Basic Science) under IBS-R012-D1. We appreciate the valuable comments on our manuscript by G. Umesh.

Authors' contributions
The author(s) read and approved the final manuscript.

Authors' information
Vishwa Bandhu Pathak is a Research Fellow at Center for Relativistic Laser Science (CoReLS), Institute for Basic Science (IBS) in Korea. After receiving Ph.D. from the Indian Institute of Technology Delhi, he worked at Group of Lasers and Plasmas in Instituto Superior Tecnico, Lisbon, Portugal. His research area of interest is intense-laser and plasma interaction, plasma-based accelerators, and laboratory astrophysics.
Seong Ku Lee is the group leader of the Ultra-Intense Laser Laboratory at the Advanced Photonics Research Institute (APRI), Gwangju Institute of Science and Technology (GIST), and the laser team leader at the Center for Relativistic Laser Science (CoReLS), Institute for Basic Science (IBS). After receiving a Ph.D. from the Korea Advanced Institute of Science and Technology, he worked at the Institute of Laser Engineering, Osaka University. He currently works at the APRI, GIST, and the CoReLS, IBS. His research field is high-power solid-state lasers.
Ki Hong Pae is a senior research scientist at Advanced Photonics Research Institute, Gwangju Institute of Science and Technology. His research field is computational laser-plasma physics. He has a high level of programming experience and has developed a relativistic particle-in-cell code with QED modules.
Calin Ioan Hojbota is a senior researcher of the Center for Relativistic Laser Science, Institute for Basic Science, Korea. He obtained his Ph.D. in physics from Gwangju Institute of Science and Technology, Korea. Before his doctoral studies, he worked at the National Institute for Research and Development of Isotopic and Molecular Technologies, Romania. His current research interests are centered around laser wakefield acceleration, with applications to laser-electron scattering, strong-field QED, and gamma photon diagnostics.
Chul Min Kim is a principal research scientist of Advanced Photonics Research Institute (APRI), Gwangju Institute of Science and Technology, Korea, and a campus research fellow of Center for Relativistic Laser Science (CoReLS), Institute for Basic Science, Korea. After receiving a Ph.D. in 2006, he has worked on X-ray lasers and relativistic laser-plasma interactions at APRI and joined CoReLS in 2012. He is interested in the theoretical analysis and computer simulation of ultra-intense light-matter interactions.
Chang Hee Nam is the director of Center for Relativistic Laser Science, Institute for Basic Science and professor of Gwangju Institute of Science and Technology, Korea. After receiving Ph.D. from Princeton University, he worked at Princeton Plasma Physics Laboratory and Korea Advanced Institute of Science and Technology until 2012.

Competing interests
The authors declare that they have no competing interests.

Author details
[1]Center for Relativistic Laser Science, Institute for Basic Science, Gwangju 61005, South Korea. [2]Advanced Photonics Research Institute, Gwangju Institute of Science and Technology, Gwangju 61005, South Korea. [3]Department of Physics and Photon Science, Gwangju Institute of Science and Technology, Gwangju 61005, South Korea.

Received: 4 January 2021 Accepted: 11 January 2021
Published online: 19 February 2021

References

1. F.J. Dyson, *Imagined Worlds* (Harvard University Press, Cambridge, 1997)
2. S.S. Schweber, *QED and the Men Who Made It: Dyson, Feynman, Schwinger, and Tomonaga* (Princeton University Press, Princeton, 1994)
3. T.H. Maiman, Nature **187**, 493 (1960)
4. W. Kaiser, C.G.B. Garrett, Phys. Rev. Lett. **7**, 229 (1961)
5. P.A. Franken et al., Phys. Rev. Lett. **7**, 118 (1961)
6. T. Brabec, F. Krausz, Rev. Mod. Phys. **72**, 545 (2000)
7. F. Krausz, M. Ivanov, Rev. Mod. Phys. **81**, 163 (2009)
8. G.A. Mourou, T. Tajima, S.V. Bulanov, Rev. Mod. Phys. **78**, 309 (2006)
9. G. Mourou, Rev. Mod. Phys. **91**, 030501 (2019)
10. E. Esarey, C.B. Schroeder, W.P. Leemans, Rev. Mod. Phys. **81**, 1229 (2009)
11. U. Teubner, P. Gibbon, Rev. Mod. Phys. **81**, 445 (2009)
12. S. Corde et al., Rev. Mod. Phys. **85**, 1 (2013)
13. A. Macchi, M. Borghesi, M. Passoni, Rev. Mod. Phys. **85**, 751 (2013)
14. T. Tajima, X.Q. Yan, T. Ebisuzaki, Rev. Mod. Plasma Phys. **4**, 7 (2020)
15. A.S. Pirozhkov et al., Opt. Express **25**, 20486 (2017)
16. Z. Guo et al., Opt. Express **26**, 26776 (2018)
17. J.W. Yoon et al., Opt. Express **27**, 20412 (2019)
18. D.A. Burton, A. Noble, Contemp. Phys. **55**, 110 (2014)
19. A. Di Piazza et al., Rev. Mod. Phys. **84**, 1177 (2012)
20. N.B. Narozhny, A.M. Fedotov, Contemp. Phys. **56**, 249 (2015)
21. The Nobel Prize in Physics 2018. https://www.nobelprize.org/prizes/physics/2018/summary/. Accessed 3 Feb 2021.
22. D. Strickland, G. Mourou, Opt. Commun. **56**, 219 (1985)
23. E. Treacy, IEEE J. Quantum Electron. **5**, 454 (1969)
24. O. Martinez, IEEE J. Quantum Electron. **23**, 59 (1987)
25. G. Cheriaux et al., Opt. Lett. **21**, 414 (1996)
26. C.P.J. Barty, C.L. Gordon, B.E. Lemoff, Opt. Lett. **19**, 1442 (1994)
27. M.D. Perry et al., Opt. Lett. **24**, 160 (1999)
28. LASER 4 ATON: 10 PW, 2 KJ. https://www.eli-beams.eu/facility/lasers/laser-4-aton-10-pw-2-kj/. Accessed 3 Feb 2021.
29. M. Aoyama et al., Opt. Lett. **28**, 1594 (2003)
30. J.H. Sung et al., Opt. Lett. **35**, 3021 (2010)
31. J.H. Sung et al., Opt. Lett. **42**, 2058 (2017)
32. W. Li et al., Opt. Lett. **43**, 5681 (2018)
33. F. Lureau et al., High Power Laser Sci. Eng. **8**, e43 (2020)
34. A. Dubietis, G. Jonušauskas, A. Piskarskas, Opt. Commun. **88**, 437 (1992)
35. V.V. Lozhkarev et al., Opt. Express **14**, 446 (2006)
36. X. Zeng et al., Opt. Lett. **42**, 2014 (2017)
37. C.N. Danson et al., High Power Laser Sci. Eng. **7**, e54 (2019)
38. S.-W. Bahk et al., Opt. Lett. **29**, 2837 (2004)
39. N.V. Didenko et al., Opt. Express **16**, 3178 (2008)
40. V. Bagnoud, F. Salin, JOSA B **16**, 188 (1999)
41. C. Hooker et al., Opt. Express **19**, 2193 (2011)
42. J. Itatani et al., Opt. Commun. **148**, 70 (1998)
43. A. Jullien et al., Opt. Lett. **30**, 920 (2005)
44. C. Thaury et al., Nat. Phys. **3**, 424 (2007)
45. I.W. Choi et al., Opt. Lett. **45**, 6342 (2020)
46. S.A. Akhmanov, A.P. Sukhorukov, R.V. Khokhlov, Sov. Phys. Uspekhi **10**, 609 (1968)
47. Hora, Heinrich, Z. Für Phys. Hadrons Nucl. **226**, 156 1969.
48. M.S. Sodha, V.K. Tripathi, Phys. Rev. A **16**, 2101 (1977)
49. E. Esarey et al., IEEE Trans. Plasma Sci. **24**, 252 (1996)
50. B.J. Duda, W.B. Mori, Phys. Rev. E **61**, 1925 (2000)
51. M. Tabak et al., Phys. Plasmas **1**, 1626 (1994)
52. J. Fuchs et al., Nat. Phys. **2**, 48 (2006)
53. I.J. Kim et al., Phys. Rev. Lett. **111**, 165003 (2013)
54. F. Albert, A.G.R. Thomas, Plasma Phys. Control. Fusion **58**, 103001 (2016)
55. V.B. Pathak, V.K. Tripathi, Phys. Plasmas **13**, 082105 (2006)
56. T. Tajima, J.M. Dawson, Phys. Rev. Lett. **43**, 267 (1979)
57. W.P. Leemans et al., Phys. Rev. Lett. **113**, 245002 (2014)
58. H.T. Kim et al., Sci. Rep. **7**, 10203 (2017)
59. S.F. Martins et al., Nat. Phys. **6**, 311 (2010)
60. I. Blumenfeld et al., Nature **445**, 741 (2007)
61. A. Macchi, *A Superintense Laser-Plasma Interaction Theory Primer*. Dordrecht: Springer Science & Business Media; 2013.
62. J. Vieira et al., New J. Phys. **12**, 045025 (2010)
63. C. Ren et al., Phys. Rev. E **63**, 026411 (2001)
64. W.B. Mori, IEEE J. Quantum Electron. **33**, 1942 (1997)
65. A. Pukhov, J. Meyer-ter-Vehn, Appl. Phys. B Lasers Opt. **74**, 355 (2002)
66. W. Lu et al., Phys. Rev. Lett. **96**, 165002 (2006)
67. W. Lu *et al.*, Phys. Rev. Spec. Top. - Accel. Beams **10**, 061301 2007.
68. S. Kiselev, A. Pukhov, I. Kostyukov, Phys. Rev. Lett. **93**, 135004 (2004)
69. S. Kneip et al., Nat. Phys. **6**, 980 (2010)
70. R. A. Fonseca *et al.*, in *Comput. Sci. — ICCS 2002*, edited by P. M. A. Sloot *et al.* (Springer Berlin Heidelberg, Berlin, Heidelberg, 2002), pp. 342–351.
71. C.D. Decker et al., Phys. Plasmas **3**, 2047 (1996)

72. I. Kostyukov et al., Phys. Rev. Lett. **103**, 175003 (2009)
73. S. Kalmykov et al., Phys. Rev. Lett. **103**, 135004 (2009)
74. V.B. Pathak et al., New J. Phys. **14**, 023057 (2012)
75. W. Leemans, E. Esarey, Phys. Today **62**, 44 (2009)
76. V. Malka *et al.*, Phys. Rev. Spec. Top. - Accel. Beams **9**, 091301 2006
77. A. Döpp et al., Phys. Plasmas **23**, 056702 (2016)
78. S. Steinke et al., Nature **530**, 190 (2016)
79. D. Kaganovich et al., Phys. Plasmas **12**, 100702 (2005)
80. J. Luo et al., Phys. Rev. Lett. **120**, 154801 (2018)
81. M. Zeng et al., Phys. Rev. Lett. **114**, 084801 (2015)
82. X.L. Xu et al., Phys. Rev. Lett. **117**, 034801 (2016)
83. M. Tzoufras et al., Phys. Rev. Lett. **113**, 245001 (2014)
84. V.B. Pathak et al., Sci. Rep. **8**, 11772 (2018)
85. A.J. Gonsalves et al., Phys. Rev. Lett. **122**, 084801 (2019)
86. J. Shin et al., Plasma Phys. Control. Fusion **60**, 064007 (2018)
87. C. Aniculaesei et al., Rev. Sci. Instrum. **89**, 025110 (2018)
88. C.I. Hojbota et al., AIP Adv. **9**, 085229 (2019)
89. C. Aniculaesei et al., Phys. Rev. Appl. **12**, 044041 (2019)
90. B.M. Hegelich et al., Nature **439**, 441 (2006)
91. H. Schwoerer et al., Nature **439**, 445 (2006)
92. P. Mora, Phys. Rev. Lett. **90**, 185002 (2003)
93. T. Esirkepov et al., Phys. Rev. Lett. **92**, 175003 (2004)
94. A. Macchi et al., Phys. Rev. Lett. **94**, 165003 (2005)
95. A. Macchi, S. Veghini, F. Pegoraro, Phys. Rev. Lett. **103**, 085003 (2009)
96. I.J. Kim et al., Phys. Plasmas **23**, 070701 (2016)
97. I.W. Choi et al., Appl. Phys. Lett. **99**, 181501 (2011)
98. F. Pegoraro, S.V. Bulanov, Phys. Rev. Lett. **99**, 065002 (2007)
99. B. Qiao et al., Phys. Rev. Lett. **105**, 155002 (2010)
100. K.H. Pae, C.M. Kim, C.H. Nam, Phys. Plasmas **23**, 033117 (2016)
101. P. Zhang et al., Phys. Plasmas **27**, 050601 (2020)
102. W. Yan et al., Nat. Photonics **11**, 514 (2017)
103. K. Poder et al., Phys. Rev. X **8**, 031004 (2018)
104. G. Sarri et al., J. Plasma Phys. **81**, 455810401 (2015)

Publisher's Note